



Stable low-temperature dry reforming of methane over mesoporous La₂O₃-ZrO₂ supported Ni catalyst

Sergey Sokolov, Evgenii V. Kondratenko, Marga-Martina Pohl, Axel Barkschat, Uwe Rodemerck*

Leibniz-Institut für Katalyse e. V. an der Universität Rostock, Albert-Einstein-Strasse 29a, D-18059, Rostock, Germany

ARTICLE INFO

Article history:

Available online 1 October 2011

Keywords:

Carbon dioxide
Methane
Synthesis gas
Dry reforming
Coke formation
Mesoporous
Macroporous

ABSTRACT

A series of supported Ni catalysts was prepared using various supports and tested in low-temperature (400 °C) dry reforming of methane. Ni/La₂O₃-ZrO₂ showed near-to equilibrium yields of CO and H₂ and the highest stability. This catalyst was studied in greater detail in order to determine the influence of the support morphology on the catalyst activity and stability. To this end, nonstructured, mesoporous, and macroporous La₂O₃-ZrO₂ were prepared and characterized before and after loading with Ni. Among them, only Ni on the mesoporous support showed practically no change in activity over 180 h on-stream, whereas the others deactivated. Formation of graphene-like coke layers on the catalysts and of NiO shell over Ni particles appears to be responsible for catalyst deactivation, while sintering of Ni did not play a major role. The enhanced stability of Ni on the mesoporous La₂O₃-ZrO₂ is attributed to stronger interaction of the Ni particles with the support stemming from a pore confinement effect.

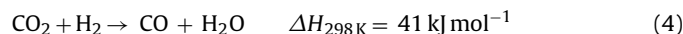
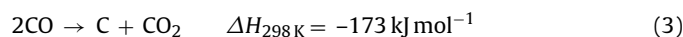
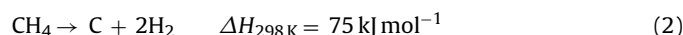
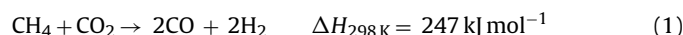
© 2011 Elsevier B.V. All rights reserved.

1. Introduction

Carbon dioxide is one of the most abundant natural sources of carbon and also a major contributor to the greenhouse effect. While reducing emissions from mobile sources, i.e. vehicles, is one of the most pressing global challenges, capturing and utilization of CO₂ from stationary sources is equally important [1]. Such sources include fossil fuel-based power plants, production of ammonia, hydrogen, cement, fertilizers and other chemicals, gas flares in oilfields or heating commercial and residential buildings etc. In general, reduction of the CO₂ emissions can be accomplished by introducing carbon-free (for example H₂-based) technologies or CO₂ capturing followed by sequestration or chemical transformations. Utilizing CO₂ as a building block for chemical processes is highly desired from the commercial and environmental points of view. Yet, developing efficient and economical processes remains one of the most challenging tasks encountered by the current catalytic research.

Dry reforming of methane (DRM) appears to be attractive for conversion of CO₂ with cheap and widely available natural gas to synthesis gas (a mixture of CO and H₂). Synthesis gas is used as a feedstock for production of methanol and for the Fischer-Tropsch reaction. The DRM reaction (Eq. (1)) is endothermic and requires high temperatures (>700 °C) for achieving industrially relevant conversions. Methane cracking (Eq. (2)), the Boudouard reaction

(Eq. (3)) and the reverse water-gas shift (RWGS) reaction (Eq. (4)) are main side reactions influencing the overall process efficiency and the catalyst long-term performance.



For the last fifteen years, dry reforming of methane has been intensively investigated with the aim to understand the reaction mechanism and to optimize the process parameters [2–5]. Supported noble metals, i.e. Rh, Ru, Ir, Pd, Pt [6–15] and Ni-based catalysts [5,16–21] showed good performance in terms of methane conversion and selectivity towards synthesis gas. However, these catalysts suffer from deactivation caused by coke deposition. The noble metal catalysts are more resistant to coking [7,14–16], while the nickel-based ones are less stable [17,22,23] but more commercially attractive because of lower cost and wider availability of nickel. For the nickel catalysts, the rate of carbon deposition was reported to decrease with rising reaction temperatures [16,24]. Recently, substantial progress in improving stability of Ni catalysts was made by employing supports like ZrO₂ [25] or La₂O₃ [5] and mixed oxides such as CaO-ZrO₂ [26,27], CeO₂-ZrO₂ and La₂O₃-ZrO₂ [28], MgAl₂O₄ [29] and others [30,31] or by embedding Ni in a mixed-metal oxide framework [32,33]. It was also demonstrated that creating zirconia-based supports having mesoporous structure improves stability of the corresponding Ni catalysts in DRM [34].

* Corresponding author. Tel.: +49 381 1281310; fax: +49 381 128151310.
E-mail address: uwe.rodemerck@catalysis.de (U. Rodemerck).

Due to the fact that high temperatures favor CH_4 and CO_2 conversion and retard coke formation, the DRM reaction was rarely investigated below 500°C . However, increasing energy costs draw our attention to a lower temperature operation. This can become economical even at moderate degrees of CH_4/CO_2 conversion provided a facile on-site recycling of educts is available. In addition, the equilibrium can be shifted towards the products by running the process in a membrane reactor where the product (hydrogen) is selectively removed from the reaction zone. Efficiency of this method was proven for the high-temperature partial oxidation of methane and methane reforming reactions [35–39]. Yet, only a few studies were dedicated to the DRM reaction below 500°C [40,41]. One drawback of the low-temperature process is thermodynamically favored coke formation by the Boudouard reaction, which results in prompt catalyst deactivation and may lead to reactor plugging.

The aim of the present study was to elucidate the effects of the support nature and morphology as well as nickel dispersion on long-term stability of nickel catalysts in DRM at 400°C . A particular attention was paid to the coke formation during the reaction and removal by temperature-programmed oxidation with O_2 or CO_2 to gain insight into the nature of the coke species.

2. Experimental

2.1. Preparation of $\text{La}_2\text{O}_3\text{-ZrO}_2$ supports

Nonstructured (LaZr-ns) and mesostructured (LaZr-meso) $\text{La}_2\text{O}_3\text{-ZrO}_2$ mixed oxides were prepared by the urea hydrolysis method according to [42]. For the LaZr-ns material, 20 g $\text{ZrO}(\text{NO}_3)_2 \cdot 2\text{H}_2\text{O}$ (Acros), 1.14 g $\text{La}(\text{NO}_3)_3 \cdot 6\text{H}_2\text{O}$ (Merck) and 30 g urea (Roth) were dissolved in 1500 mL of distilled water. The synthesis mixture for LaZr-meso material contained the same amounts of reactants plus 30 g of Pluronic P123 (Aldrich) amphiphilic block copolymer. In both cases, a white precipitate was formed during stirring at 95°C for 48 h. The precipitate was isolated by filtration, washed with a small amount of distilled water, dried at room temperature, and calcined in flowing air at 500°C for 5 h (heating rate 5 K/min).

$\text{La}_2\text{O}_3\text{-ZrO}_2$ with macropore skeleton (LaZr-macro) was prepared by a templated synthesis using poly(methyl methacrylate) (PMMA) colloidal crystals as macropore molds. Pluronic F127 (Aldrich) block copolymer was added to the solution in the attempt to create a hierarchically porous structure where mesopores penetrate macropore walls. 10 mL of zirconium acetate solution in diluted acetic acid (2.22 mol/L , Aldrich) were mixed with 10 mL of methanol. In this mixture, 1.26 g of $\text{La}(\text{NO}_3)_3 \cdot 6\text{H}_2\text{O}$ (Merck) and 1 g of Pluronic F127 (Aldrich) were dissolved. PMMA colloidal crystals (ca. 7 g) were soaked in the solution for 10 min and the excess of the solution was removed by filtration. The infiltrated colloidal crystals were dried at room temperature under vacuum for 14 h and then calcined in flowing air using the following temperature profile: $2\text{ K/min} \rightarrow 350^\circ\text{C}$ holding for 2 h $\rightarrow 2\text{ K/min} \rightarrow 600^\circ\text{C}$ holding for 4 h. PMMA spheres were synthesized by surfactant-free emulsion polymerization as reported elsewhere [43]. Colloidal crystals of PMMA spheres were formed upon slow drying (ambient conditions) of the aqueous suspension. The average sphere size obtained from scanning electron micrographs was $408 \pm 12\text{ nm}$.

2.2. Preparation of the catalysts

In addition to the above $\text{La}_2\text{O}_3\text{-ZrO}_2$ supports, several commercial oxide and hydrous oxide carriers were used in this study. The BET surface areas of the calcined supported catalysts based on SiO_2 , Al_2O_3 (Degussa, alumina C), $\text{SiO}_2\text{-Al}_2\text{O}_3$ (Sasol, Siral 10), TiO_2

(Degussa, P25), MgO (Alfa Aesar), $\text{Al}_x\text{Mg}_{1-x}\text{O}_y$ (Condea, Pural MG30), $\text{Zr}(\text{O})\text{OH}$ (MEL), and $\text{La}_2\text{O}_3\text{-ZrO}_2$ (MEL) were 366, 79, 254, 6, 1.1, 183, 25, and $65\text{ m}^2/\text{g}$, respectively. The catalysts based on the commercial supports were prepared by excess-solution impregnation using a synthesis robot (Zinsser GmbH, Germany). Under vigorous shaking, 5.5 mL of aqueous nickel nitrate solution were dosed to each of the pre-shaped supports (2 g, particle size $310\text{--}710\text{ }\mu\text{m}$) followed by drying at 100°C for 2.5 h. The LaZr-ns and LaZr-meso supports were impregnated according to the same procedure. The nickel nitrate concentration in the impregnation solution was set to yield 5 wt.% of Ni in a calcined catalyst. To verify the loading, catalysts supported on $\text{La}_2\text{O}_3\text{-ZrO}_2$ were analyzed by ICP. Ni content on the commercial $\text{La}_2\text{O}_3\text{-ZrO}_2$ was 4.2 wt.%, while LaZr-ns and LaZr-meso had 4.3 and 4.2 wt.% respectively. Ni loading in other catalysts should be in a similar range. Dried precursors were calcined in a muffle furnace in static air at 650°C for 5 h.

Robot-assisted preparation was not applied for Ni/LaZr-macro catalyst in order to preserve macroporous support structure, which could partially collapse during vigorous shaking. 0.232 g of LaZr-macro were added to 2 mL of 0.1 M aqueous nitrate solution at ambient temperature. The material was dried in static air at 65°C for 14 h and then calcined in a continuous flow quartz reactor in air at 650°C for 5 h (40 mL/min per 100 mg of calcined solid).

2.3. Catalyst characterization

Morphology of the calcined catalysts was analyzed by scanning electron microscopy (SEM) on JEOL 7401F operated between 4.0 and 10.0 kV . Their specific surface area was measured by nitrogen physisorption at -196°C on BELSORP-mini II (BEL Japan, Inc.) applying the Brunauer, Emmet and Teller (BET) method. X-ray diffraction patterns of the pure supports and calcined catalysts were collected on a STADI P automated transmission diffractometer (STOE, Germany) with an incident beam curved germanium monochromator selecting $\text{CuK}\alpha_1$ radiation ($\lambda = 1.5406\text{ \AA}$) and a 6° linear position sensitive detector. The alignment was checked by a silicon standard. The data were collected in the 2θ range from 10° to 60° with a step size of 0.5° and a measurement time of 50 s per step. The phase composition of the samples was determined using the program suite WINXPow by STOE&CIE with inclusion of the Powder Diffraction File PDF2 of the ICDD (International Centre of Diffraction Data). The elemental composition of the supports and catalysts was determined by inductively coupled plasma optical emission spectroscopy (ICP-OES, Varian 715-ES). The surface composition was studied by X-ray photoelectron spectroscopy (XPS). The spectra were recorded on a VG ESCALAB 220iXL instrument with monochromatic $\text{Al K}\alpha$ radiation ($E = 1486.6\text{ eV}$). The peaks were fitted by Gaussian–Lorentzian curves after Shirley or Tougaard background subtraction. The electron binding energy was referenced to the C1s peak at 284.8 eV . For quantitative analysis of the near-surface region, the peak areas were determined and divided by the element-specific Scofield factors and the analyzer-dependent transmission function.

Ni particles supported on $\text{La}_2\text{O}_3\text{-ZrO}_2$ were analyzed before and after the DRM reaction by transmission electron microscopy (TEM). To come close to the state of Ni particles in fresh catalysts, they were reduced following the same procedure as in the actual catalytic experiment (Section 2.4). After reduction, the samples were cooled to room temperature in N_2 flow, which was then gradually changed to an $\text{N}_2:\text{O}_2=80:20$ flow. TEM measurements were performed at 200 kV on JEM-ARM200F (JEOL) aberration-corrected by a CESCOR (CEOS) for the scanning transmission (STEM) applications. The microscope was equipped with a JED-2300 (JEOL) energy-dispersive X-ray (EDX) spectrometer for chemical analysis. High-angle annular dark field (HAADF) and EDX mapping were performed with a spot size of 5 c and $40\text{ }\mu\text{m}$ condenser aperture.

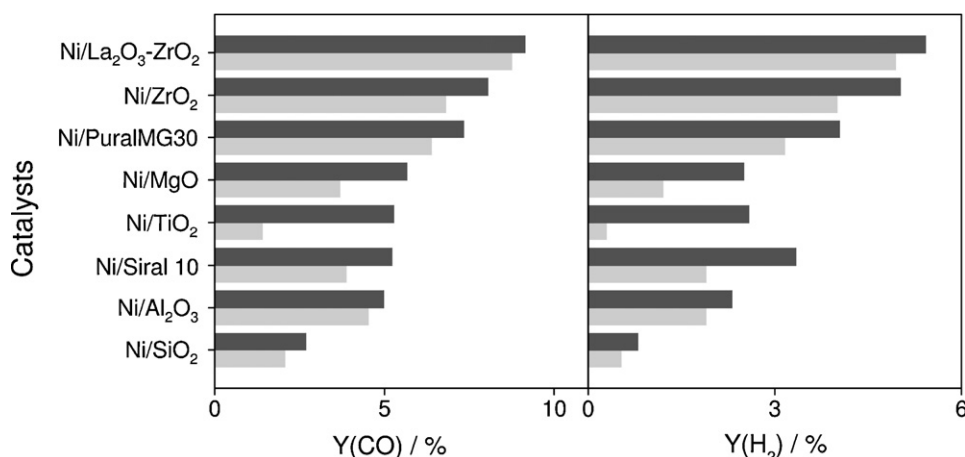


Fig. 1. CO and H₂ yields obtained after first 1–10 h (black bars) and 100 h (gray bars) on-stream over selected catalysts in DRM at 400 °C and GHSV of 7200 mL h⁻¹ g_{cat}⁻¹.

Sample preparation was done by depositing powders directly on a holey carbon film supported on Cu-grid (mesh 300).

Temperature-programmed oxidation (TPO) measurements were performed with samples having been used in the DRM reaction at 400 °C for 100 h. The materials (100 mg) were heated with 20 K/min up to 850 °C in a mixture of 5% O₂ in Ar with a total flow rate of 100 mL/min. Oxygen consumption and formation of reaction products were monitored by a quadrupole mass spectrometer (Pfeiffer Vacuum OmniStar). The following atomic mass units (AMUs) were analyzed: 44 (CO₂), 40 (Ar), 32 (O₂), 28 (CO, CO₂), and 18 (H₂O). The concentrations of O₂ and CO₂ were determined from the respective AMUs using standard fragmentation patterns and sensitivity factors. In the CO₂-TPO experiments, used catalysts were heated to 800 °C with 20 K/min rate in CO₂ (5 vol.%) in Ar with a total flow rate of 100 mL/min.

Temperature-programmed reduction (TPR) measurements were performed with calcined samples as follows. The materials were heated to 800 °C at 10 K/min rate in a gas mixture of 10% H₂ in N₂ with a total flow rate of 12 mL/min. Hydrogen (AMU 2) consumption and formation of water (AMU 18) were monitored by the quadrupole mass spectrometer. Sensitivity factors for MS fragments were derived from a series of calibrations performed on reference gas mixtures.

2.4. Catalytic tests

Catalytic tests were performed in a parallel reactor system consisting of 50 single fixed-bed continuous flow reactors (quartz tubes, inner diameter of 4 mm) assembled in an electrically heated oven. The calcined materials (50 or 100 mg, particle size of 310–710 μm) were diluted with silicon carbide particles (750 mg, 500–710 μm) for improved heat transfer and heat distribution through the catalyst bed. Before testing in the DRM reaction, the catalysts were reduced in a mixture of 10% H₂ in N₂ at 650 °C for 14 h. After flushing with nitrogen and cooling down to reaction temperature, a CH₄:CO₂:N₂ = 10:10:80 mixture was fed to the reactors with a flow rate of 12 mL/min per reactor. DRM tests were carried out at 400 °C at gas hourly space velocity (GHSV) of 7200 mL h⁻¹ g_{cat}⁻¹. To verify stability of Ni/LaZr-meso, it was additionally tested at GHSV of 14,400 mL h⁻¹ g_{cat}⁻¹ ensuring CH₄/CO₂ conversions lower than at thermodynamic equilibrium. The feed components and reaction products were quantitatively analyzed using an Agilent 7890A gas chromatograph equipped with HP-Plot Q and Molsieve 5A columns (Ar carrier gas) for separation of CO₂, H₂O, H₂, N₂, and CO and with Al₂O₃/K column (He carrier gas) for CH₄. Thermal conductivity and flame ionization detectors were

used for quantifying the permanent gases and methane, respectively.

3. Results

3.1. Catalytic performance

CO, H₂ and H₂O were the main reaction products of DRM at 400 °C over all studied catalysts. Fig. 1 compares the yields of hydrogen and carbon monoxide formed in the DRM reaction over different catalysts after first 1–10 h (black bars) and after 100 h (gray bars) on-stream. Despite the fact that Ni/SiO₂ possessed the highest specific surface area, it showed the lowest initial yield of H₂ followed by Ni/Al₂O₃, Ni/MgO and Ni/TiO₂. Taking into account the rather low surface area (1.1 m²/g) of Ni/MgO catalyst, the achieved initial H₂ yield of 2.5% is remarkable. Ni supported on mixed-metal oxides (Ni/Siral 10 and Ni/PuralMG30) showed significantly higher initial activity compared to the corresponding Ni catalysts supported on Al₂O₃, SiO₂, and MgO. The highest initial activities were measured over the catalysts that contain Zr in the support. The H₂ yield reached 5% over Ni/ZrO₂ and further increased to 5.4% when ZrO₂ was promoted with La₂O₃. CO yields also shown in Fig. 1 were generally higher than those of H₂ over all tested catalysts. This is due to the fact that additional CO was formed in a RWGS reaction from CO₂ and H₂. The occurrence of this reaction was confirmed by presence of water among the products and by the fact that CO₂ conversion was higher than that of CH₄.

For further evaluation of the catalysts, we compared the initial H₂ yields with those after 100 h on DRM stream (Fig. 1, gray bars). This comparison gives insight into the catalyst resistance against deactivation. The TiO₂-supported catalyst showed 89% loss of the initial activity, while Ni/Al₂O₃, Ni/PuralMG30, and Ni/ZrO₂ lost 20%. The highest stability was found for Ni/La₂O₃-ZrO₂, who lost only 9%.

Thus, the catalytic performance of nickel in the low-temperature DRM reaction strongly depends on the nature of supporting materials. In view of the high initial activity and time-on-stream stability of Ni/La₂O₃-ZrO₂, we investigated this catalytic system in greater detail. A particular emphasis was placed on elucidating the effect of the support morphology on the catalytic performance. To this end, we first examined La content, micro- and mesostructure of commercial La₂O₃-ZrO₂ (Table 1) and then synthesized mixed oxides with similar La/Zr ratio and microstructure but different morphology. These oxides were used for preparing Ni catalysts as described in Sections 2.1 and 2.2. Their time on-stream performance in the DRM reaction is summarized in Fig. 2. Ni supported on nonstructured La₂O₃-ZrO₂ (Ni/LaZr-ns) showed high initial yields of both

Table 1

Diameter (D_p) and volume (V_p) of pores, crystallite size (CZ), content of La and Ni in pristine La_2O_3 - ZrO_2 supports as well as amount of carbon removed by O_2 ($\text{C}(\text{O}_2\text{-TPO})$) and CO_2 ($\text{C}(\text{CO}_2\text{-TPO})$) from the corresponding Ni/ La_2O_3 - ZrO_2 catalysts having been used in the DRM reaction at 400 °C for 100 h.

Materials	D_p , nm	S_{BET} , m^2/g	V_p , cm^3/g	CZ ^c , nm	La ^d , wt.%	Ni ^d , wt.%	$\text{C}(\text{O}_2\text{-TPO})$, $\text{mg}/\text{g}_{\text{cat}}$	$\text{C}(\text{CO}_2\text{-TPO})$, $\text{mg}/\text{g}_{\text{cat}}$
LaZr-ns	3 ^a	79	0.09	14	3.8	4.3	5	4
LaZr-meso	3 and 5 ^a	83	0.12	11	4.1	4.2	14	20
LaZr-macro	274 ^b	33	–	8	6.4	3.4	42	47
LaZr-MEL	5.6 ^a	94	0.23	14	6.4	4.2		

^a From N_2 adsorption.

^b From SEM measurement.

^c From XRD using the Scherrer equation at 2θ of 30°.

^d From ICP.

hydrogen (4.8%) and carbon monoxide (8.7%). Same as for Ni on other supports, the yield of CO was higher compared to that of H_2 due to RWGS reaction. The yields of both products decreased with time; 20–25% of the initial activity was lost after 100 h on-stream. Considerably higher initial yields of H_2 (5.6%) and CO (10.5%) were obtained over Ni/LaZr-macro (macroporous La_2O_3 - ZrO_2). However, the catalyst deactivation rate was rather similar to that observed over Ni/LaZr-ns. In contrast, Ni/LaZr-meso (mesoporous La_2O_3 - ZrO_2) retained its activity almost entirely for at least 180 h on-stream. Moreover, the catalyst activity did not decrease over 100 h on-stream when the DRM reaction was performed at a higher GHSV, i.e. at CH_4 conversion significantly lower than at the equilibrium (Fig. 2). It even slightly increased over the first 20 h of the experiment, however, rationalizing this phenomenon is out-with the scope of the current study. Therefore, we conclude that Ni/LaZr-meso shows high intrinsic stability against deactivation.

3.2. Morphology and structure of La_2O_3 - ZrO_2 resulting from different preparation methods

X-ray diffraction pattern of commercial La_2O_3 - ZrO_2 corresponds to tetragonal ZrO_2 phase (PDF#00-079-1769) and gave an average crystallite size of 14 nm calculated from the reflection at 2θ of 30° using the Scherrer equation. The nitrogen gas adsorption experiment showed type IV isotherm indicating mesoporous structure of the material. A maximum on Barrett–Joyner–Halenda (BJH) plot corresponded to a pore diameter of 5.6 nm; the BET surface area was 94 m^2/g .

Fig. 3a shows an SEM image of the external surface of nonstructured mixed metal oxide (LaZr-ns), which is mainly composed of sintered and irregularly shaped 35–90 nm plates. Some of the particles were crushed on a sample holder in order to compare the inner and the outer structures. The morphology found on the split

of the particle (Fig. 3b) differed significantly from the one observed on the outer surface. The bulk of the particles consisted of stacked 20–30 nm platelets scarcely penetrated by 2–3 nm pores. The LaZr-ns sample showed type IV isotherm confirming the presence of mesopores as seen in the SEM micrographs in Fig. 3a and b. One maximum on BJH plot corresponded to a pore diameter of 3 nm, the BET surface area was 79 m^2/g (Table 1). The X-ray diffraction pattern of LaZr-ns is shown in Fig. S1 and corresponded to ZrO_2 tetragonal phase (PDF#79-1769) with an average crystallite size of 14 nm.

LaZr-meso also prepared by the urea hydrolysis method, but in presence of amphiphilic block copolymer (P123) micelles appeared optically similar to LaZr-ns. However, their morphology was different as proven by SEM analysis. The external surface of a LaZr-meso particle shown in Fig. 3c consisted of spherical grains of 15–35 nm, sintered but with visible openings between them. The inner structure observed on a broken particle was highly porous with pores apparently cast by the organic micelles, though disordered (Fig. 3d). The oxide grains found inside the particle had spherical shape and were 6–10 nm in size, i.e. significantly smaller than on the external surface of the particle. As in case of LaZr-ns, type IV isotherm was observed in the N_2 adsorption experiment, yet there were two maxima on the BJH-plot corresponding to 3 and 5 nm pore diameters. However, the use of mesostructure templates did not result in a substantial increase in the specific surface area, which in case of LaZr-meso amounted to 83 m^2/g . The X-ray diffractogram of LaZr-meso (Fig. S1) contains only reflections of the same tetragonal zirconia phase as in commercial La_2O_3 - ZrO_2 or LaZr-ns. However, LaZr-meso average crystallite size of 11 nm was somewhat smaller.

The third type of La_2O_3 - ZrO_2 support prepared with the use of macro- and mesostructure templates created a network of interconnected macropores organized in ordered arrays (Fig. 3e).

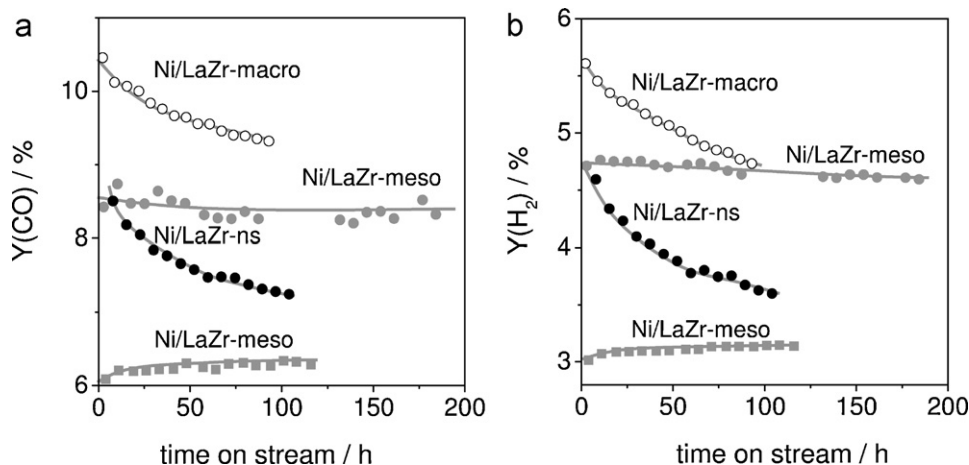


Fig. 2. Time on-stream yields of (a) CO and (b) H_2 obtained over Ni/LaZr-ns, Ni/LaZr-meso and Ni/LaZr-macro in DRM at 400 °C at GHSV of 7200 $\text{mL h}^{-1} \text{g}_{\text{cat}}^{-1}$. For Ni/LaZr-meso, an additional measurement at GHSV of 14,400 $\text{mL h}^{-1} \text{g}_{\text{cat}}^{-1}$ is added (gray squares).

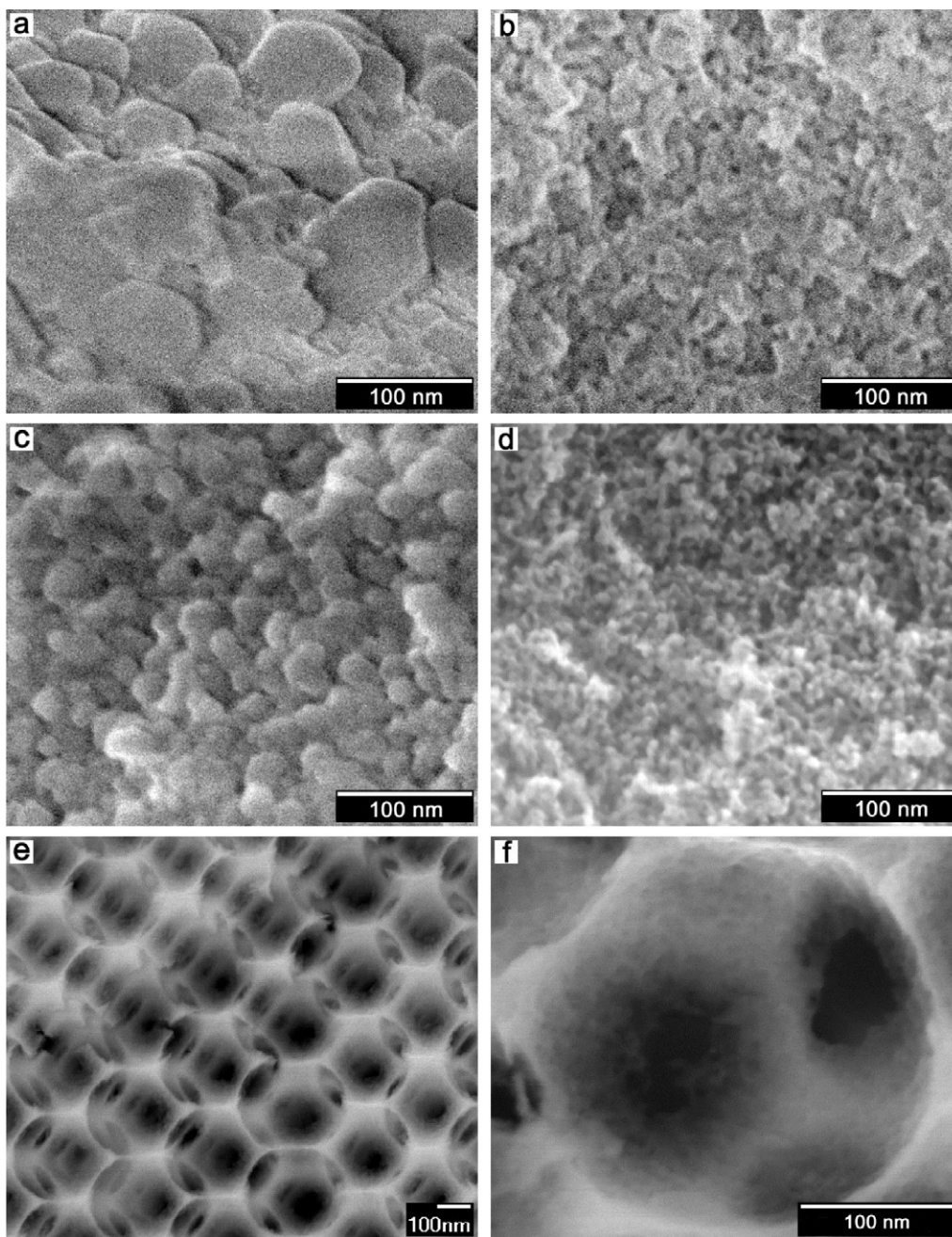


Fig. 3. SEM images of the $\text{La}_2\text{O}_3\text{-ZrO}_2$ supports prepared in this study. (a) Surface of LaZr-ns; (b) crushed LaZr-ns particle; (c) surface of LaZr-meso; (d) crushed LaZr-meso particle; (e) macropore arrangement in LaZr-macro; (f) mesostructure of the macropore walls of LaZr-macro.

The average pore size derived from measuring pore openings in the LaZr-macro micrographs was 274 ± 25 nm indicating 33% shrinkage from the average size of PMMA latex, which is typical for three-dimensionally ordered macroporous oxides [44]. Examined at higher magnification, macropore walls revealed textural features most likely imprinted by the F127 micelles, however, well-defined mesopores were not observed (Fig. 3f). It is not clear if PMMA colloidal crystals voids furnish right conditions for micelles self-assembly during solvent evaporation. Nitrogen adsorption showed type II isotherm and gave BET surface area of $33 \text{ m}^2/\text{g}$. XRD analysis detected the same tetragonal phase as in LaZr-ns and LaZr-meso (Fig. S1). The average crystallite size of 8 nm found in LaZr-macro is the smallest among the three materials despite higher calcination temperature used to fully remove PMMA template (600°C for LaZr-macro vs. 500°C for

LaZr-ns and LaZr-meso). One reason for such difference is found in the specifics of crystallite sintering mechanism characteristic for three-dimensionally ordered macroporous (3DOM) crystalline materials [45]. In particular, the cross dimensions of the 3DOM network structural elements, such as “beams” connecting the “nodes” (octahedral and tetrahedral holes in PMMA colloidal crystals), are on the same order of size as the crystallites. Hence, the crystallites building the 3DOM skeleton, especially its thinner elements (“beams”), will have fewer immediate neighbors than in an ordinary bulk material and consequently a lower sintering rate.

Commercial $\text{La}_2\text{O}_3\text{-ZrO}_2\text{-MEL}$, LaZr-ns, -meso and -macro were analyzed by XPS to determine a surface content of La and Zr and compare to the values obtained by ICP. For all materials, La/Zr ratios derived from ICP and XPS were very similar or identical indicating

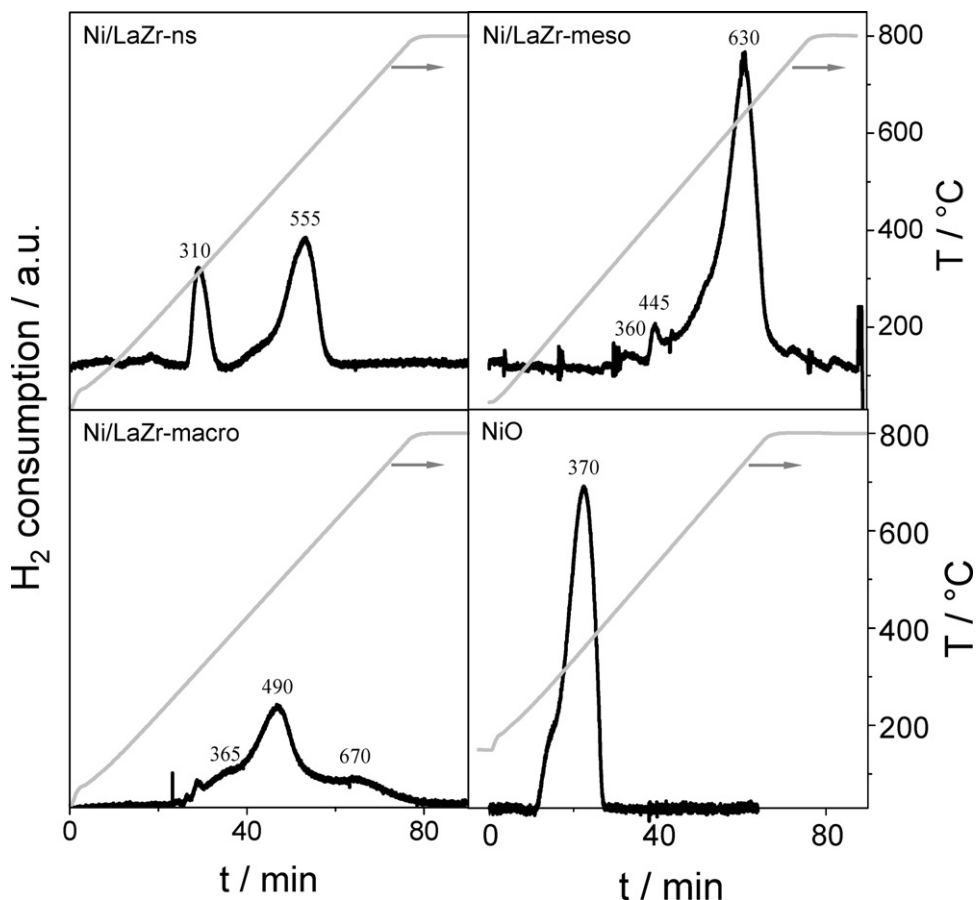


Fig. 4. H_2 -TPR profiles of Ni/LaZr-ns, Ni/LaZr-macro, Ni/LaZr-meso and of bulk NiO.

that no surface enrichment with La occurred during supports preparation (Table S1).

3.3. Redox properties of Ni/La₂O₃-ZrO₂

The H_2 -TPR profiles of the differently prepared Ni/La₂O₃-ZrO₂ materials are shown in Fig. 4. T_{max} , which qualitatively reflects the reducibility of the supported nickel oxide, depends strongly on the supporting material. Ni/LaZr-ns showed distinct maxima of H_2 consumption at 310 and 555 °C and an additional shoulder at 445 °C. This indicates that different NiO_x species exist in this material. The H_2 -TPR profile of Ni/LaZr-macro also consists of several, however, less-resolved maxima of H_2 consumption at 365, 490, and 670 °C. In contrast, Ni/LaZr-meso possesses predominantly NiO_x species, which are characterized by T_{max} at 630 °C. In addition, there are comparatively low fractions of others reduced at T_{max} of 360 and 445 °C. To gain insight into the nature of NiO_x species on different La₂O₃-ZrO₂ supports, we performed H_2 -TPR tests over pure NiO calcined in air at 800 °C for 2 h. As seen from Fig. 4, the reduction of NiO starts at 270 °C while the main reduction peak is at 370 °C. A small shoulder at 310 °C may be ascribed to the reduction of NiO surface. Previously Biswas and Kunzru [46] reported that a NiO/ZrO₂ catalyst containing bulk NiO (Ni content of 30 wt.%) showed H_2 consumption in a similar temperature range with a maximum at 344 °C. Based on this report and the reduction profile of bulk NiO, we suggest that Ni/LaZr-ns and Ni/LaZr-macro possess bulk-like NiO aggregates in addition to surface-dispersed NiO_x species, while Ni/LaZr-meso contains predominantly dispersed NiO_x with only a small fraction of larger species.

3.4. TEM study of fresh Ni/La₂O₃-ZrO₂ catalysts

To observe Ni particles in the state they appear on fresh (before the DRM reaction) catalysts, they were reduced according to the standard protocol for catalytic tests (Section 2.4) and studied by TEM. EDX elemental maps of Ni and Zr and their corresponding HAADF images of Ni/LaZr-ns, Ni/LaZr-meso and Ni/LaZr-macro catalysts are shown in Fig. 5a–c, respectively. Due to the low atomic weight contrast between Ni and Zr and similar morphology of the support and Ni particles, nickel species are not distinct on STEM bright field (not shown) or HAADF images of Ni/LaZr-ns and Ni/LaZr-meso. Only in case of Ni/LaZr-macro where La₂O₃-ZrO₂ crystallites are small, some Ni particles appear as spherical bright spots on thinner fragments of macroporous support. However, EDX elemental mapping reveals areas with high Ni content in all three catalysts. Such areas may consist of a single or multiple particles mostly exposed (green) or partially shielded by La₂O₃-ZrO₂ crystallites (yellow). Although randomly selected catalyst fragments cannot be fully representative of the entire material, there are indications that Ni particle size varies in a wide range in Ni/LaZr-ns and -meso. According to the EDX elemental mapping Ni particle size ranges between 3.0 and 11.6 with a maximum at 5.4 nm in Ni/LaZr-ns, while for Ni/LaZr-meso respective values were 4.2, 26.1, and 8.6 nm. More uniformly sized (from 6.1 to 22.4 nm) Ni particles with a slightly bigger average size of 11.1 nm were found on LaZr-macro. Being morphologically well resolved on macroporous support, Ni particles were also measured on TEM and SEM images (Figs. S2 and S7a). The averages of 10.7 nm found by TEM and 10.0 by SEM are in a good agreement with the EDX-derived value.

High resolution TEM investigation that followed EDX mapping was carried out to shed light on possible decoration of Ni

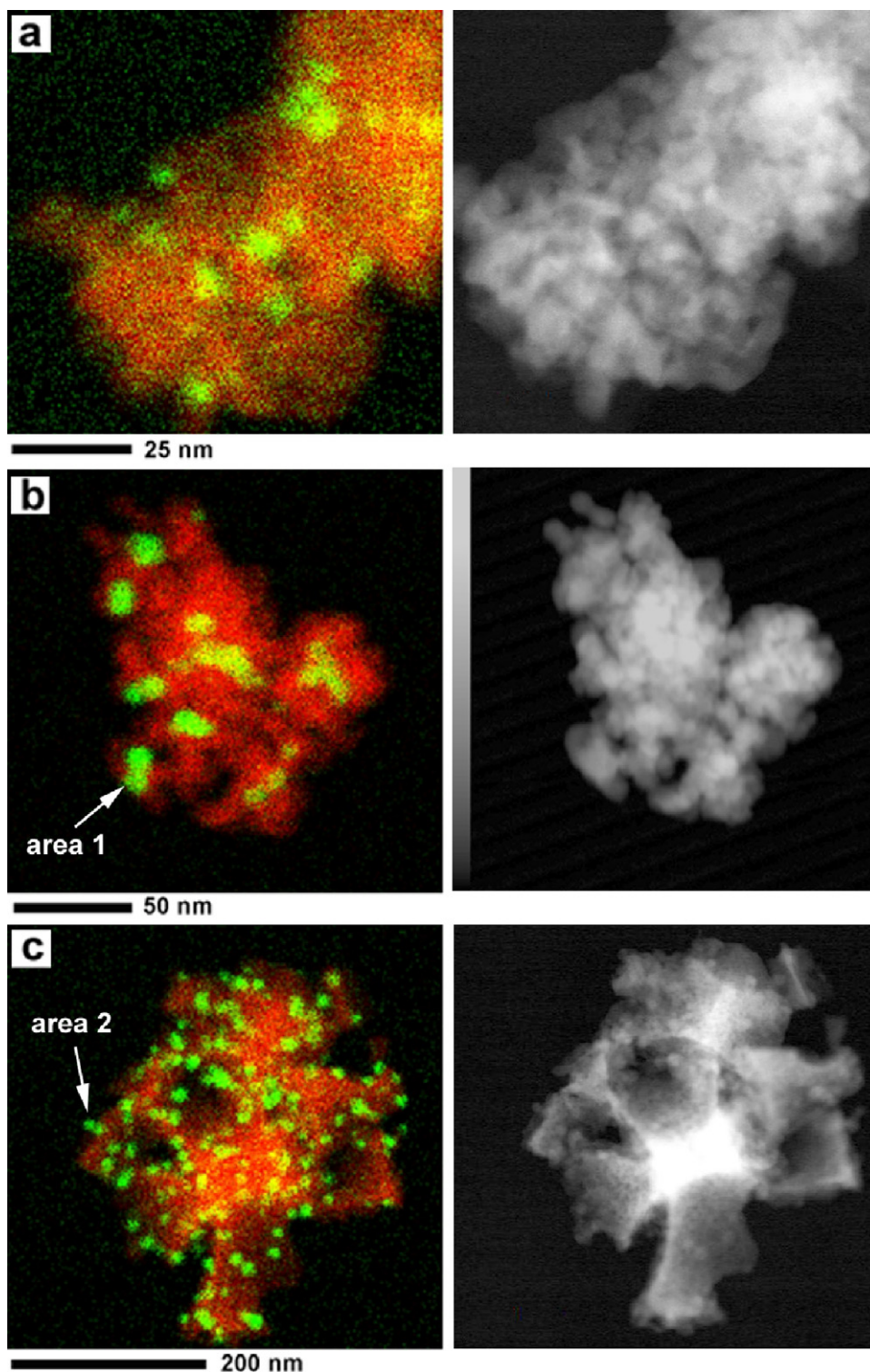


Fig. 5. EDX elemental maps (left column) and corresponding HAADF images (right column) of reduced Ni/LaZr-ns (a), Ni/LaZr-meso (b) and Ni/LaZr-macro (c). On elemental maps, red color corresponds to Zr, green to Ni. Yellow color results from mixing signals from the two elements. (For interpretation of the references to color in this figure legend, the reader is referred to the web version of the article.)

particles with La_2O_3 . To accomplish it, we thoroughly searched for Ni particles with minimal shielding from La_2O_3 - ZrO_2 crystallites. Unfortunately, such particles were identified only in meso- and macro-structured Ni/LaZr but not in Ni/LaZr-ns. Fig. 6a shows the TEM image of a practically unshielded Ni particle found on Ni/LaZr-meso in area 1 marked in Fig. 5b. Using selected two pixels marked by arrows, an inverse FFT reconstruction returned a nickel

particle seen on the high resolution TEM image. The distance between atomic planes measured on the inverse FFT image was 2.06 Å, which corresponds to the 111 plane of cubic Ni (2.04 Å, PDF#65-380). Area 2 of Ni/LaZr-macro contained a Ni particle substantially free of foreign crystallites (Fig. 6b). Inverse FFT of pixels indicated by arrows reconstructed a pattern of lattice planes found in the first quadrant of the particle circumference. The interplanar

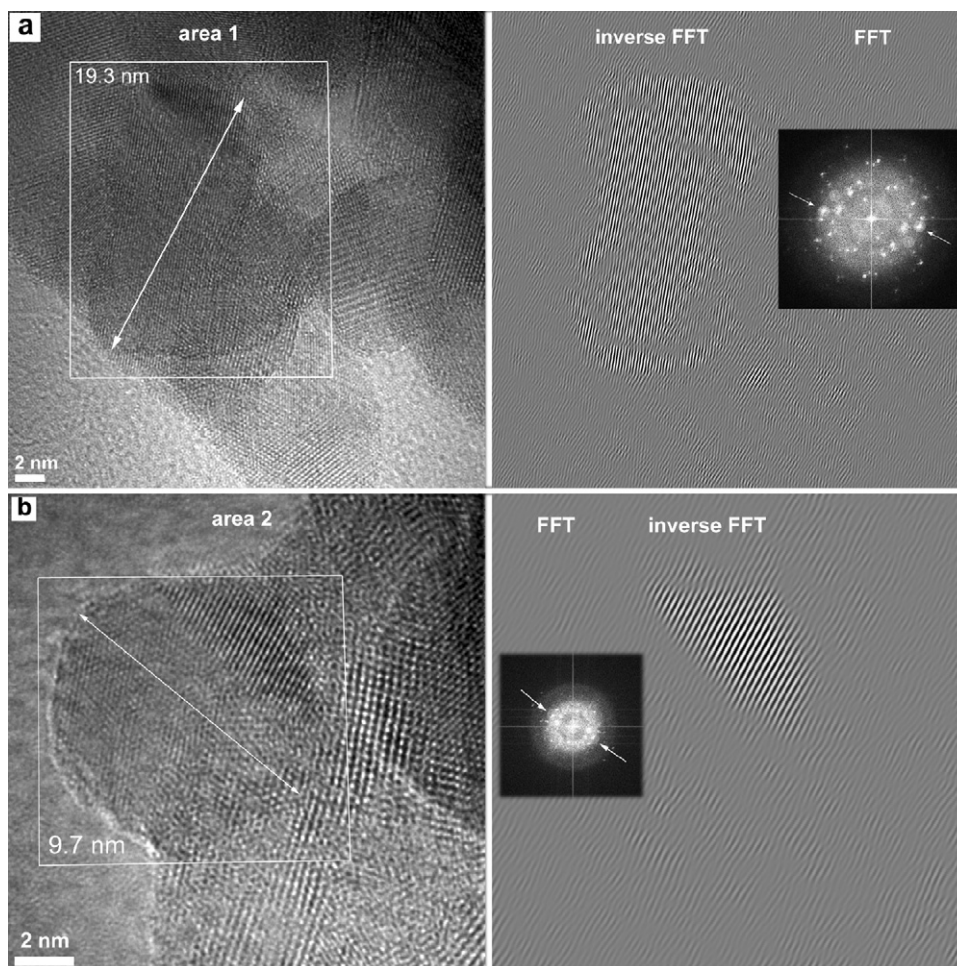


Fig. 6. High resolution TEM images of Ni particles in area 1 on Ni/LaZr-meso with corresponding FFT and inverse FFT (a), and area 2 on Ni/LaZr-macro with corresponding FFT and inverse FFT (b). Reflections used for inverse FFT are marked by arrows.

distance of 2.00 Å closely matches the 101 plane of hexagonal Ni (2.01 Å, PDF#89-7129).

Selected areas of a Ni/LaZr-macro fragment with clearly distinct Ni particles were analyzed by EDX. One spot analyzed was confined to the Ni particle (Fig. S3, area 001) and the other laid on the support away from the particle (area 002). In EDX spectra Ni appeared as the major element in area 001, although certain amounts of Zr and La were also present. Area 002 contained Zr and La, while only trace amount of Ni was detected. Appearance of Zr and La in area 001 may indicate that the Ni particle is shielded by some support crystallites on the side of electron beam incidence and/or that EDX penetration depth exceeds the particle thickness and the support from under the Ni particle is also probed by the method. Apparently, precise composition of Ni particles in this size range cannot be determined by EDX, hence we could not decidedly conclude whether Ni particles are decorated by lanthana.

3.5. Temperature-programmed oxidation of used Ni/La₂O₃-ZrO₂ catalysts

In order to verify if carbonaceous deposits are formed during the DRM reaction and whether they can be oxidatively removed, we performed temperature-programmed oxidation of Ni/La₂O₃-ZrO₂ materials having been used in the DRM reaction at 400 °C for 100 h. O₂ was applied as oxidizing agent in these experiments. CO₂ and H₂O were the main products, while CO was formed only in trace quantities. Fig. 7 compares the profiles of CO₂ measured during

the TPO tests over different Ni/La₂O₃-ZrO₂ catalysts. The amount of carbon removed from 100 mg of each catalyst was calculated by integrating the CO₂ profiles and is listed in Table 1. Ni/LaZr-macro contained the highest amount of coke followed by Ni/LaZr-meso and Ni/LaZr-ns. The materials differ not only in the amount but also in the nature of carbon species as derived from the CO₂ profiles possessing several maxima. For Ni/LaZr-macro, the main peak of CO₂ formation appears at 547 °C while a group of smaller ones clusters around 770 °C. The CO₂ profile of Ni/LaZr-meso is characterized by two distinct maxima at 416 and 680 °C as well as by three less resolved ones at 173, 277, and 815 °C. Only a small peak at 727 °C and two tiny peaks at lower temperature were identified in the CO₂ profile of Ni/LaZr-ns.

In order to test if carbonaceous deposits can be removed by CO₂ under DRM conditions, TPO with CO₂ (CO₂-TPO) was also performed over the catalysts having been used in the DRM reaction at 400 °C for 100 h.

Fig. 8 compares the profiles of CO₂ consumption during the course of CO₂-TPO experiments on Ni/LaZr-ns, Ni/LaZr-meso, and Ni/LaZr-macro. For quantifying these experiments, it was suggested that one CO₂ molecule removes one carbon atom. Thus, the amount of removed carbon was calculated by integrating the profiles of CO₂ consumption. The obtained values are listed in Table 1. Again, the Ni/LaZr-macro catalyst consumed the greatest amount of CO₂ starting at 450 °C and reaching maximum at 560 °C. Smaller fraction of coke reacted with CO₂ at higher temperatures up to the highest applied of 800 °C. The Ni/LaZr-meso catalyst revealed the

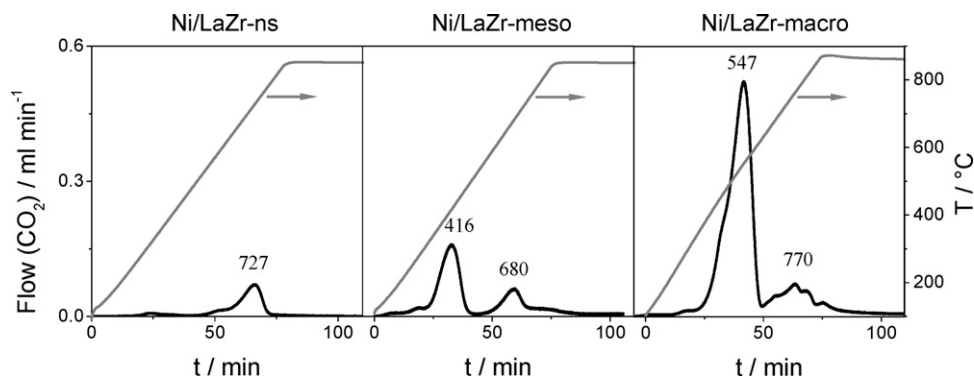


Fig. 7. CO₂ profiles obtained upon TPO of used Ni/LaZr-ns, Ni/LaZr-meso and Ni/LaZr-macro with O₂ (20 K/min, 850 °C 2 h).

second highest amount of carbonaceous deposits removed by CO₂. Compared to Ni/LaZr-macro, the CO₂ profile of Ni/LaZr-meso is broader and characterized by the onset at 415 °C and the maximum at 590 °C. This sample also showed CO₂ consumption at temperature as low as 275 °C, but in much smaller quantities. The Ni/LaZr-ns catalyst consumed the lowest amount of CO₂ starting above 500 °C, i.e. at the highest temperature among the three catalysts.

3.6. TEM study of used Ni/La₂O₃-ZrO₂ catalysts

In order to observe possible transformations of Ni particles and to study carbonaceous deposits formed, Ni/LaZr catalysts were examined by TEM after 100 h on-stream in DRM. Ni particles were detected by EDX elemental mapping on all three used catalysts. In case of Ni/LaZr-ns and Ni/LaZr-meso, the number of particles found was unfortunately insufficient for a valid statistical evaluation of the particle size (Fig. S4). Fig. 9 shows EDX elemental mapping of Ni/LaZr-macro with its corresponding HAADF image (panels a and b respectively). Comparing the EDX maps of the fresh (Fig. 5c) and used (Fig. 9) catalysts suggests that no significant change of Ni dispersion occurred over the 100 h DRM test. Measurements performed on the TEM image shown in Fig. 9c gave an average particle size of 10.1 nm, which is very close to 10.7 nm found on the fresh catalyst. SEM analysis of the used sample (Fig. S7b) returned a value of 9.9 nm confirming that no significant change in Ni particle size occurred.

Close inspection of Ni particles on the TEM image of Ni/LaZr-macro in Fig. 9 revealed that some of them have core-shell structure. On the two particles found in area 3 such structure could be examined in greater detail. Crystalline lattice planes in the core and shell of the particle 1 can be clearly observed on a high-resolution micrograph of this area (Fig. 9d). FFT of this micrograph

followed by the inverse operation performed on selected pixels returned lattice planes found only in the shell of the particle 1 (Fig. S5). The interplanar distance of 2.40 Å calculated from the inverse FFT indicates that the shell contains NiO. However, the exact NiO phase is difficult to assign since all known NiO lattice systems (cubic, PDF#47-1049; rhombohedral, PDF#89-3080; monoclinic, PDF#65-6920) contain this interplanar distance. Since such core-shell structures were not found on freshly reduced Ni/LaZr-macro, we can assume that a layer of NiO was formed on some Ni particles in the course of DRM test.

Fig. 10a clearly illustrates that after 100 h DRM test, Ni/LaZr-ns contained carbon in form of filaments and irregularly shaped particles. In addition, the catalyst particles were partially coated by carbon deposits with layered structure typical for graphenes (marked by arrows in Fig. 10b). Such deposits were also detected directly on a Ni particle removed from the support by grown filaments (Fig. S6a). In case of Ni/LaZr-meso, no graphene layers were found on the catalyst particles. However, carbon filaments crowned with metallic Ni particles were abundant (Fig. 10c, Fig. S6b).

Thorough examination of used Ni/LaZr-macro did not reveal filamentous carbon. EDX carbon map of the catalyst fragment examined earlier for Ni and Zr content (Fig. 9a) showed a continuous coverage of the catalyst with carbon that must have originated from the DRM reaction (Fig. S8). Selected areas of another catalyst fragment also partially exposed through an opening in the carbon film were examined by EDX (Fig. S6c). A spot selected roughly in the middle of the catalyst particle showed 42 at% of carbon suggesting that a relatively thick coke layer was formed on the catalyst (Fig. S6c, area 003). Establishing the nature of coke species on Ni/LaZr-macro was, however, difficult. On a high resolution TEM image shown in Fig. 10d, a coat of amorphous material (marked by arrows) is discernable on the crystalline support and

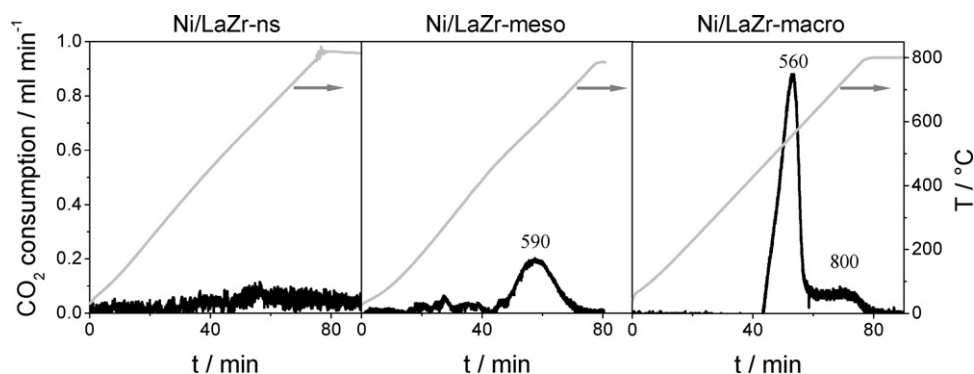


Fig. 8. CO₂ profiles obtained upon TPO of used Ni/LaZr-ns, Ni/LaZr-meso and Ni/LaZr-macro with CO₂ (20 K/min, 800 °C 2 h).

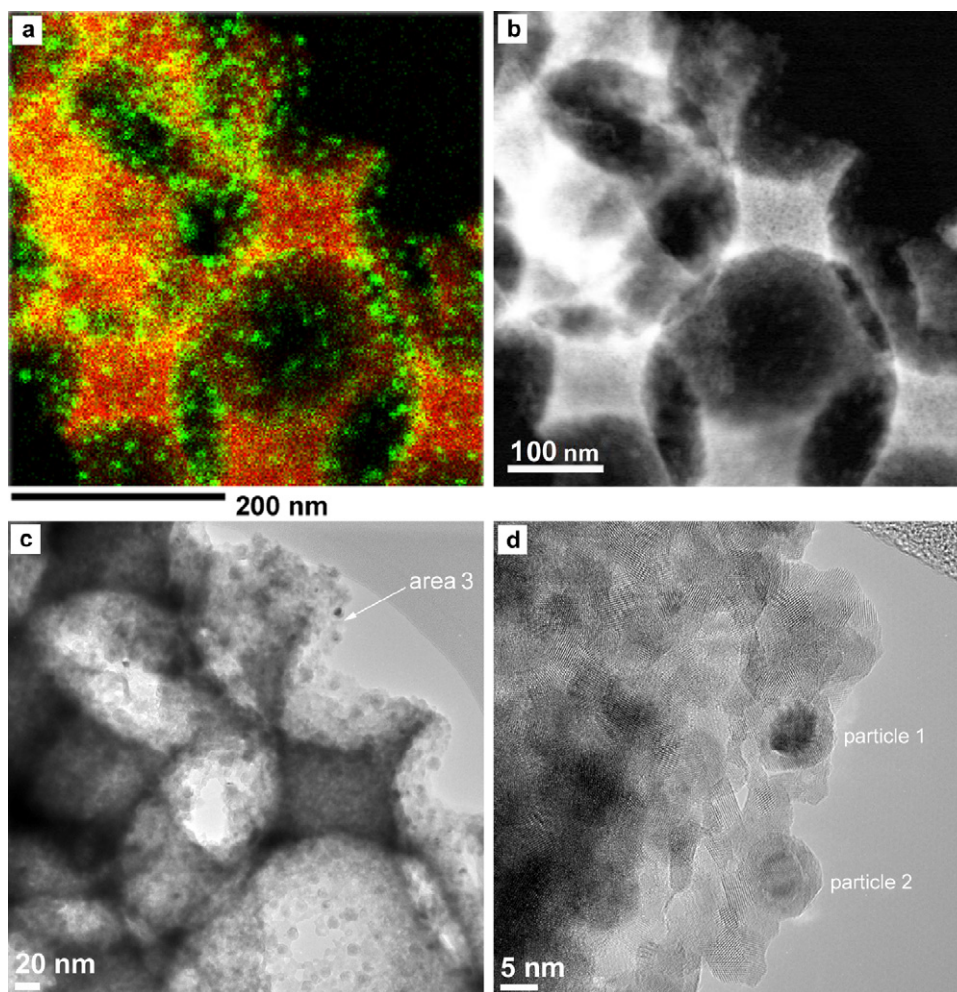


Fig. 9. EDX elemental map of used Ni/LaZr-macro (a) and a corresponding HAADF image (b). Higher magnification TEM images used for measuring the average Ni particle size (c) and for studying the structure of core-shell particles (d).

Ni particles, but it lacks a well-defined layered structure as seen on Ni/LaZr-ns.

4. Discussion

The results of previous catalytic studies of the high-temperature ($\geq 700^\circ\text{C}$) DRM reaction on supported Ni catalysts [2,3,30] are discussed and compared with the present results to elucidate the effect of nature and morphology of the supports on catalyst activity and stability in low-temperature (400°C) DRM reaction. No prior knowledge exists for this temperature regime. In general, chemical nature of a support material plays a major role both in forming active Ni metal particles and in the reaction mechanism. Ni/SiO₂, which exhibited the lowest activity in the current study (Fig. 1), has also been shown to be a poor catalyst at higher temperatures [47]. Its low activity was attributed to the low Ni dispersion as a result of weak binding of NiO_x species to the support. When mixed SiO₂-Al₂O₃ oxides were used as a support, a higher Ni dispersion was achieved thanks to stronger interaction of NiO_x with the support [47]. In fact, Ni/Siral10 in the present study showed much higher activity than both Ni/SiO₂ and Ni/Al₂O₃, while the highest activities in low-temperature DRM were found for Ni/La₂O₃-ZrO₂, Ni/ZrO₂, and Ni/PuralMG30 (Fig. 1). These findings are in accordance with the DRM activity trends observed at higher temperature, e.g. $>650^\circ\text{C}$. Basic elements like alkaline-earth metals or lanthanides were shown to enhance activity by two

mechanisms: (i) enhancing nickel-support interaction resulting in higher nickel dispersion and (ii) activating CO₂ by forming carbonates [2,3,32]. The latter effect was also observed over unpromoted ZrO₂, which possesses neither acidic nor basic properties [48].

The highest stability among the most active supported catalysts in the present study was found for Ni/La₂O₃-ZrO₂ (Fig. 1). According to [34], high stability of La₂O₃-supported Ni catalysts in high-temperature DRM is due to suppressing coke formation by enhancing CO₂ concentration at the basic La sites and thus accelerating the Boudouard reaction towards CO. This mechanism may also play a role at low temperature. The same coke removal mechanism, but directly from Ni particles supported on La₂O₃ was proposed by Slagtern et al. [49]. The authors demonstrated that Ni particles are decorated by La₂O₃ species, which create CO₂ adsorption sites amid CH₄ activation sites, i.e. Ni atoms. As a result, carbon formed from methane on Ni can be removed more efficiently thus extending lifetime of the catalyst. Such decoration may also occur on Ni/La₂O₃-ZrO₂ catalysts prepared for the current study. However, our thorough TEM analysis of these catalysts did not provide an insight into Ni particles decoration.

Despite the fact that our Ni/La₂O₃-ZrO₂ catalysts show comparable initial activity, their stability strongly depends on the support structure (Fig. 2). Ni/LaZr-meso did not lose its activity over 180 h on-stream, while Ni/LaZr-ns and Ni/LaZr-macro showed a drop in their activity with similar deactivation trends. Such difference is remarkable taking into account very similar chemical nature of the

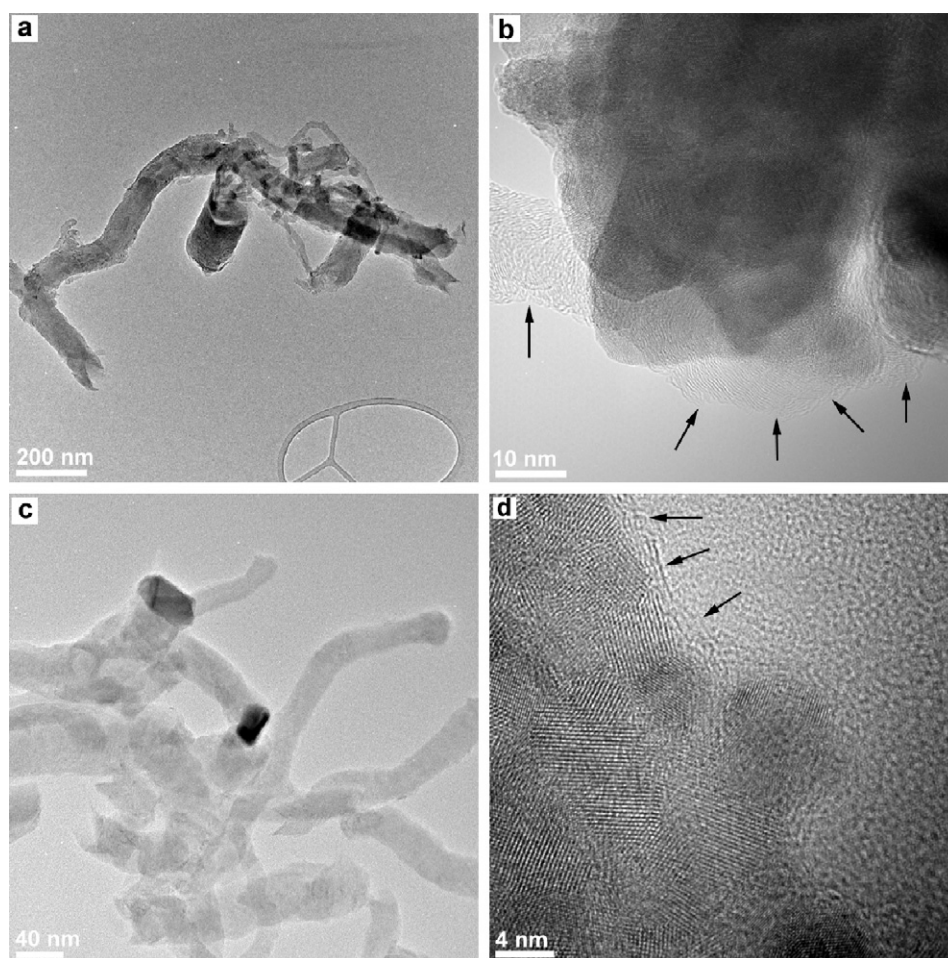


Fig. 10. TEM images of carbon filaments (a) and graphene layers (b, marked by arrows) observed on used Ni/LaZr-ns; TEM image of carbon filaments with attached Ni particles observed on used Ni/LaZr-meso (c); TEM image of used Ni/LaZr-macro with carbon layers are marked by arrows (d).

supports. From a mechanistic point of view, the loss of the catalyst activity in a high-temperature DRM reaction is usually explained either by coking, reduction of Ni dispersion through particle sintering, oxidation of metallic nickel particles, or a combination thereof. In the following discussion we try to identify possible mechanistic origins governing time on-stream performance of Ni supported on differently structured $\text{La}_2\text{O}_3\text{-ZrO}_2$.

Our combined TEM and SEM analyses have shown that Ni particle size on macroporous $\text{La}_2\text{O}_3\text{-ZrO}_2$ remained practically unchanged through the DRM experiment (Sections 3.4 and 3.6). Hence sintering can be excluded as a possible reason for deactivation of Ni/LaZr-macro. The same should be valid for Ni/LaZr-ns since TPR experiments proved that NiO_x -support interaction on Ni/LaZr-ns is similar to Ni/LaZr-macro. Therefore, Ni sintering behavior on the nonstructured catalyst should be also similar to Ni/LaZr-macro, i.e. negligible or no sintering. Since sintering is impeded by strengthening NiO_x -support interactions [47], no Ni sintering should occur on Ni/LaZr-meso exhibiting significantly stronger NiO_x -support interaction compared to Ni/LaZr-ns and Ni/LaZr-macro. Actually, the Ni/LaZr-meso showed very high stability in our DRM test (Fig. 2).

It is worth mentioning that core-shell Ni/NiO particles were formed on Ni/LaZr-macro during the course of 100 h DRM experiment, while no such particles were identified on Ni/LaZr-meso showing very stable performance. Therefore, according to [50], such reaction-induced oxidation of Ni to NiO appears to be responsible for the deactivation of Ni/LaZr-macro. Although due to low contrast we were not able to observe core-shell Ni/NiO particles

on Ni/LaZr-ns, which deactivated at a similar rate as Ni/LaZr-macro (Fig. 2), we cannot exclude a possibility of their formation on this catalyst.

Another factor influencing catalysts on-stream stability is formation of coke. As demonstrated in Section 3.5, the Ni/La $_2\text{O}_3$ -ZrO $_2$ catalysts strongly differed in the amount and nature of carbon-containing species formed in the course of 100 h DRM reaction carried out at 400 °C. These species could be removed both by oxygen and carbon dioxide (Table 1, Figs. 7 and 8). Briefly, the most active Ni/LaZr-macro deposited the highest amount of coke. Oxidation of this coke by O $_2$ and CO $_2$ started at 350 and 450 °C respectively, and most of it was removed below 600 °C with both oxidants. In addition, there exist certain coke species burned in O $_2$ at higher temperature with a maximum at ca. 750 °C. Similar to Ni/LaZr-macro, Ni/LaZr-ns also formed carbon species that were removed with O $_2$ at higher temperature with a maximum at 727 °C. TEM revealed graphene layers on the catalyst particles and filamentous carbon (Fig. S5a). Graphenes are known as coke species reducing catalyst activity by blocking active nickel sites [51]. Furthermore, not all carbon deposited on Ni/LaZr-ns reacted with CO $_2$, which indicates that 400 °C DRM reaction does not creates favorable conditions for removal of encapsulating coke. The most stable Ni/LaZr-meso formed the second highest amount of carbonaceous deposits. 70% of them were oxidized by O $_2$ below 500 °C with a maximum at 416 °C. Compared to O $_2$, CO $_2$ was not so efficient in removing these species. Nevertheless, we suggest that carbon removal with CO $_2$ proceeds under the current DRM conditions (400 °C) for the following reasons. We should recall that:

(i) increasing the temperature at 20 K/min rate in the CO₂-TPO experiments shifts the “C” + CO₂ reaction events to higher temperatures compared to the isothermal conditions of the DRM reaction and (ii) the contact time in the DRM reaction was 8 times longer than in the CO₂-TPO experiments. Obviously, the probability for reacting CO₂ with carbon species increases with the contact time. We suggest that the concentration of the low-temperature burning coke species does not change under steady-state conditions and is determined by the rates of their formation and consumption via the Boudouard reaction. Graphene layers were not found on Ni/LaZr-meso by TEM analysis. Instead, carbon filaments were found. Facetted Ni particles topping off the filaments did not exhibit core-shell structure and had lattice spacing characteristic of metallic Ni. Such particles were shown to remain active in CH₄ cracking and CO₂ dissociation even when removed from the support [52].

In summary, we attribute high stability of Ni/LaZr-meso in 400 °C DRM to the properties of Ni particles shaped by mesoporous structure of the support during the catalyst preparation. Strong Ni-support interaction on Ni/LaZr-meso apparently retards formation of graphene layers and makes Ni particles more resistant to oxidation thus rendering the catalyst stable. One possible explanation of the role played by the support mesostructure in enhancing metal-support interaction is partial confinement of NiO_x particles to the mesopores resulting in a greater fraction of a given particle surface chemically bound to La₂O₃-ZrO₂.

5. Conclusions

A series of Ni-containing (ca. 5 wt.%) catalysts was prepared using various supports and tested in low-temperature (400 °C) dry reforming of methane to synthesis gas. Under the applied reaction conditions, Ni/La₂O₃-ZrO₂ catalysts showed near-to equilibrium yields of CO and H₂. However, their DRM performance strongly depended on the morphology of La₂O₃-ZrO₂ support provided that all supports possessed the same tetragonal crystalline phase. Nickel supported on the mesoporous La₂O₃-ZrO₂ showed practically no change in activity over 180 h on-stream. In contrast, the catalysts based on nonstructured and macroporous La₂O₃-ZrO₂ lost approximately 20% of their initial activity over 100 h on-stream. The two phenomena responsible for the catalyst deactivation were formation of graphene layers covering Ni particles and of NiO shells on Ni particles.

The effect of the support morphology on the DRM performance was ascribed to the nature of NiO_x species formed during the catalysts preparation step. While the less stable catalysts possessed a variety of NiO_x particles, including weakly bound bulk-like NiO, highly dispersed and stronger bound NiO_x species were present on the mesoporous support. Resulting Ni particles also had stronger interaction with this support and were more resistant to deactivation by graphitic carbon and oxidation than Ni particles on non-structured and macro-porous supports. Enhanced Ni-support interaction on mesoporous La₂O₃-ZrO₂ possibly arises from partial encapsulation of NiO_x species by mesopores during the catalyst preparation and, as a result, formation and endurance of chemical bonding with greater portion of each Ni particle in subsequent steps.

Acknowledgements

Financial support by German Ministry of Education and Research (BMBF, contract no. 03X216) in the “ACENET ERA-NET” European framework is gratefully acknowledged. The authors thank M. Marschall and K. Buchholz for technical assistance in the catalytic experiments as well as V. Gölden (TPR, TPO), A. Simmulla (ICP), J. Radnik (XPS), and M. Schneider (XRD) for carrying out catalyst characterization.

Appendix A. Supplementary data

Supplementary data associated with this article can be found, in the online version, at doi:10.1016/j.apcatb.2011.09.035.

References

- [1] C. Song, *Catal. Today* 115 (2006) 2–32.
- [2] M.C.J. Bradford, M.A. Vannice, *Catal. Rev.* 41 (1999) 1–42.
- [3] Y.H. Hu, E. Ruckenstein, B.C. Gates, H. Knoezinger (Eds.), *Advances in Catalysis*, Academic Press, 2004, pp. 297–345.
- [4] S. Wang, G.Q. Lu, G.J. Millar, *Energy Fuels* 10 (1996) 896–904.
- [5] X.E. Verykios, *Int. J. Hydrogen Energy* 28 (2003) 1045–1063.
- [6] J.T. Richardson, S.A. Paripatyadar, *Appl. Catal.* 61 (1990) 293–309.
- [7] A.T. Ashcroft, A.K. Cheetham, M.L.H. Green, P.D.F. Vernon, *Nature* 352 (1991) 225–226.
- [8] A. Erdöhelyi, J. Cserenyi, F. Solymosi, *J. Catal.* 141 (1993) 287–299.
- [9] F. Solymosi, G. Kutsán, A. Erdöhelyi, *Catal. Lett.* 11 (1991) 149–156.
- [10] J.R. Rostrup-Nielsen, J.H.B. Hansen, *J. Catal.* 144 (1993) 38–49.
- [11] A. Erdöhelyi, J. Cserenyi, E. Papp, F. Solymosi, *Appl. Catal. A* 108 (1994) 205–219.
- [12] J. Nakamura, K. Aikawa, K. Sato, T. Uchijima, *Catal. Lett.* 25 (1994) 265–270.
- [13] V.A. Tsipouriari, A.M. Efstathiou, Z.L. Zhang, X.E. Verykios, *Catal. Today* 21 (1994) 579–587.
- [14] Z.L. Zhang, V.A. Tsipouriari, A.M. Efstathiou, X.E. Verykios, *J. Catal.* 158 (1996) 51–63.
- [15] A.M. Efstathiou, A. Kladi, V.A. Tsipouriari, X.E. Verykios, *J. Catal.* 158 (1996) 64–75.
- [16] A.M. Gadalla, B. Bower, *Chem. Eng. Sci.* 43 (1988) 3049–3062.
- [17] J.R. Rostrup-Nielsen, D.M. Bibby, C.D. Chang, R.F. Howe, S. Yurchak, *Stud. Surf. Sci. Catal.* 36 (1988) 73–78.
- [18] D. Liu, R. Lau, A. Borgna, Y. Yang, *Appl. Catal. A* 358 (2009) 110–118.
- [19] Z. Hou, O. Yokota, T. Tanaka, T. Yashima, *Appl. Catal. A* 253 (2003) 381–387.
- [20] J. Juan-Juan, M.C. Román-Martínez, M.J. Illán-Gómez, *Appl. Catal. A* 355 (2009) 27–32.
- [21] S. Therdthianwong, C. Siangchin, A. Therdthianwong, *Fuel Process. Technol.* 89 (2008) 160–168.
- [22] Z.L. Zhang, X.E. Verykios, *Catal. Today* 21 (1994) 589–595.
- [23] Y. Matsumura, T. Nakamori, *Appl. Catal. A* 258 (2004) 107–114.
- [24] A.M. Gadalla, M.E. Sommer, *Chem. Eng. Sci.* 44 (1989) 2825–2829.
- [25] Q.-H. Zhang, Y. Li, B.-Q. Xu, *Catal. Today* 98 (2004) 601–605.
- [26] J.D.A. Bellido, J.E. De Souza, J.-C. M'Peko, E.M. Assaf, *Appl. Catal. A* 358 (2009) 215–223.
- [27] J.D.A. Bellido, E.M. Assaf, *Appl. Catal. A* 352 (2009) 179–187.
- [28] S.M. Staggs-Williams, F.B. Noronha, G. Fendley, D.E. Resasco, *J. Catal.* 194 (2000) 240–249.
- [29] L. Gucci, G. Stefler, O. Geszti, I. Sajó, Z. Pászti, A. Tompos, Z. Schay, *Appl. Catal. A* 375 (2010) 236–246.
- [30] M.S. Fan, A.Z. Abdullah, S. Bhatia, *ChemCatChem* 1 (2009) 192–208.
- [31] A.P.E. York, T.-C. Xiao, M.L.H. Green, J.B. Claridge, *Catal. Rev.* 49 (2007) 511–560.
- [32] A. Olafsen, C. Daniel, Y. Schuurman, L.B. Råberg, U. Olsbye, C. Mirodatos, *Catal. Today* 115 (2006) 179–185.
- [33] G. Valderrama, A. Kiennemann, M.R. Goldwasser, *Catal. Today* 133–135 (2008) 142–148.
- [34] M. Rezaei, S.M. Alavi, S. Sahebdelfar, P. Bai, X. Liu, Z.-F. Yan, *Appl. Catal. B* 77 (2008) 346–354.
- [35] A. Santos, J. Coronas, M. Menedez, J. Santamaria, *Catal. Lett.* 30 (1995) 189–199.
- [36] E. Kikuchi, Y. Chen, M. de Pontes, R.L. Espinoza, C.P. Nicolaidis, J.H. Scholtz, M.S. Scurrrell, *Stud. Surf. Sci. Catal.* 107 (1997) 547–553.
- [37] A.K. Prabhu, R. Radhakrishnan, T.S. Oyama, *Appl. Catal. A* 183 (1999) 241–252.
- [38] P. Ferreira-Aparicio, I. Rodríguez-Ramos, A. Guerrero-Ruiz, *Appl. Catal. A* 237 (2002) 239–252.
- [39] J. Múnera, S. Irusta, L. Cornaglia, E. Lombardo, *Appl. Catal. A* 245 (2003) 383–395.
- [40] P. Ferreira-Aparicio, A. Guerrero-Ruiz, I. Rodríguez-Ramos, *Appl. Catal. A* 170 (1998) 177–187.
- [41] S. Irusta, L.M. Cornaglia, E.A. Lombardo, *J. Catal.* 210 (2002) 263–272.
- [42] S. Pengpanich, V. Meeyoo, T. Rirksomboon, K. Bunyakiat, *Appl. Catal. A* 234 (2002) 221–233.
- [43] D. Munro, A.R. Goodall, M.C. Wilkinson, K. Randle, J. Hearn, *J. Colloid Interface Sci.* 68 (1979) 1–13.
- [44] B.T. Holland, C.F. Blanford, T. Do, A. Stein, *Chem. Mater.* 11 (1999) 795–805.
- [45] S. Sokolov, D. Bell, A. Stein, *J. Am. Ceram. Soc.* 86 (2003) 1481–1486.
- [46] P. Biswas, D. Kunzru, *Int. J. Hydrogen Energy* 32 (2007) 969–980.
- [47] M. Houalla, B. Delmon, *J. Phys. Chem.* 84 (1980) 2194–2199.
- [48] J.H. Bitter, K. Seshan, J.A. Lercher, *J. Catal.* 171 (1997) 279–286.
- [49] A. Slagtern, Y. Schuurman, C. Leclercq, X. Verykios, C. Mirodatos, *J. Catal.* 172 (1997) 118–126.
- [50] S. Slagtern, U. Olsbye, R. Blom, I.M. Dahl, R.L.E.C.P.N.J.H.S.M. de Pontes, M.S. Scurrrell (Eds.), *Studies in Surface Science and Catalysis*, Elsevier, 1997, pp. 497–502.
- [51] A. Effendi, K. Hellgardt, Z.G. Zhang, T. Yoshida, *Catal. Commun.* 4 (2003) 203–207.
- [52] V.C.H. Kroll, H.M. Swaan, S. Lacombe, C. Mirodatos, *J. Catal.* 164 (1996) 387–398.